LETTER

doi:10.1038/nature11554

Synaptic amplification by dendritic spines enhances input cooperativity

Mark T. Harnett[1]*, Judit K. Makara[1,2]*, Nelson Spruston[1], William L. Kath[3] & Jeffrey C. Magee[1]

Dendritic spines are the nearly ubiquitous site of excitatory synaptic input onto neurons[1,2] and as such are critically positioned to influence diverse aspects of neuronal signalling. Decades of theoretical studies have proposed that spines may function as highly effective and modifiable chemical and electrical compartments that regulate synaptic efficacy, integration and plasticity[3–8]. Experimental studies have confirmed activity-dependent structural dynamics and biochemical compartmentalization by spines[9–12]. However, there is a longstanding debate over the influence of spines on the electrical aspects of synaptic transmission and dendritic operation[3–8,13–18]. Here we measure the amplitude ratio of spine head to parent dendrite voltage across a range of dendritic compartments and calculate the associated spine neck resistance (R_{neck}) for spines at apical trunk dendrites in rat hippocampal CA1 pyramidal neurons. We find that R_{neck} is large enough (~500 MΩ) to amplify substantially the spine head depolarization associated with a unitary synaptic input by ~1.5- to ~45-fold, depending on parent dendritic impedance. A morphologically realistic compartmental model capable of reproducing the observed spatial profile of the amplitude ratio indicates that spines provide a consistently high-impedance input structure throughout the dendritic arborization. Finally, we demonstrate that the amplification produced by spines encourages electrical interaction among coactive inputs through an R_{neck}-dependent increase in spine head voltage-gated conductance activation. We conclude that the electrical properties of spines promote nonlinear dendritic processing and associated forms of plasticity and storage, thus fundamentally enhancing the computational capabilities of neurons[19–21].

To measure the ratio of spine-to-dendrite voltage amplitude and associated R_{neck}, we combined two-photon Ca^{2+} imaging and glutamate uncaging with dual dendritic patch-clamp current injection and voltage recording from hippocampal CA1 pyramidal neurons in acute slices from adult rats. Excitatory input was produced by uncaging onto a single spine of interest located on the apical dendritic trunk. The resulting excitatory postsynaptic potential (EPSP) was measured in the dendritic branch (termed $EPSP_{branch}$; see Methods), and laser power was modulated to generate a range of $EPSP_{branch}$ amplitudes and associated spine head Ca^{2+} signals (assayed via the calcium indicator dye Oregon Green 488 BAPTA-1 (OGB-1)) that were mediated exclusively by voltage-gated Ca^{2+} channels (Fig. 1b, e, f; 0.5–1.0 μM tetrodotoxin (TTX) and 50–100 μM D(-)-2-amino-5-phosphonovaleric acid (AP5) present; Supplementary Figs 2–4). Next, excitatory postsynaptic current (EPSC)-shaped currents were injected into the dendrite to depolarize the spine to a level at which the associated spine Ca^{2+} signals matched those produced by the glutamate uncaging (Fig. 1c–f and Supplementary Fig. 9) (8.6 ± 1.0 μm between pipettes, 14.2 ± 1.7 μm from spine of interest to voltage-recording electrode). Owing to the lack of voltage attenuation from the dendrite to the spine[3,4,6], these dendritic depolarizations provide an accurate estimate of the amplitude of uncaging-evoked spine head potentials (termed $EPSP_{spine}$; see Methods). The amount of electrical compartmentalization produced by the spine was measured as the amplitude ratio (AR) of $EPSP_{spine}$ to $EPSP_{branch}$. R_{neck} was subsequently calculated from this value and the measured dendritic impedance (11.0 ± 1.0 MΩ, $n = 8$ cells; equation (4) in Methods).

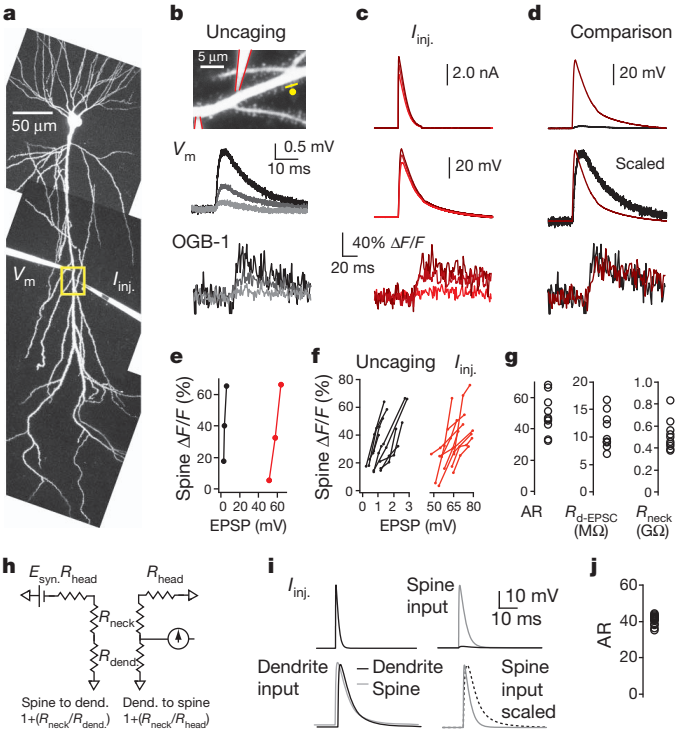

Figure 1 | Measurement of voltage amplitude ratio across apical trunk spine necks. **a**, Two-photon *Z*-stack image of a CA1 pyramidal neuron patched with two electrodes at the apical trunk ~200 μm from the soma. **b**, Top, yellow box from **a** expanded to show spine imaging (yellow line) and two-photon glutamate-uncaging (yellow dot) locations. Electrodes are outlined in red. Middle, averaged voltage traces and bottom, spine Ca^{2+} signals evoked by uncaging at increasing laser powers. **c**, EPSC-shaped waveforms delivered through one electrode ($I_{inj.}$, top) evoked EPSPs recorded at the other electrode (V_m, middle) and spine Ca^{2+} signals (bottom). **d**, Comparison of voltage traces (top, actual amplitude; middle, scaled) corresponding to similar spine Ca^{2+} signals (bottom). **e**, Spine Ca^{2+} signals versus EPSP amplitude evoked by single-spine glutamate uncaging (black) and EPSC injection (red) for the cell shown in **a**–**d**. **f**, Summary of ten experiments comparing single trunk spine uncaging with current injection during dual dendritic recording. **g**, AR calculated from $EPSP_{spine}/EPSP_{branch}$ at comparable spine Ca^{2+} signals (left) for experiments shown in **f** and associated peak dendritic input resistance during EPSC injection ($R_{d\text{-}EPSC}$; middle) were used to derive R_{neck} (right). **h**, Circuit diagram for voltage attenuation from dendrite-to-spine versus spine-to-dendrite across spine head, spine neck, and dendritic resistances. **i**, Voltage responses at the dendrite (black) or spine head (grey) in a multi-compartment model of a CA1 neuron for a trunk spine 213 μm from the soma with a 500 MΩ R_{neck} in response to fast current injection at either the spine head or dendrite. **j**, Summary of AR for 18 model trunk spines located 150–300 μm from the soma.

[1]HHMI Janelia Farm Research Campus, Ashburn, Virginia 20147, USA. [2]Institute of Experimental Medicine, Hungarian Academy of Sciences, Budapest 1083, Hungary. [3]Departments of Applied Mathematics and Neurobiology, Northwestern University, Evanston, Illinois 60208, USA.
*These authors contributed equally to this work.

For apical trunk spines located 223 ± 10 µm from the soma we measured an AR of 49.0 ± 3.8 and corresponding R_{neck} of 514 ± 44 MΩ ($n = 10$ spines from 8 cells; Fig. 1g). A morphologically realistic multi-compartmental simulation using an R_{neck} of 500 MΩ for trunk spines at similar locations supported the above observations (Fig. 1i, j). Under physiological conditions, the mean unitary dendritic EPSP amplitude at these synapses is ~0.5 mV[22]. Together with our measurements above, this reported value suggests spine head depolarizations of ~25 mV for an average unitary event. These data indicate that spines function as high-impedance input compartments that passively amplify synaptic depolarization locally within the spine head to well over what could be achieved by synapses directly onto dendrites. Thus, unitary synaptic inputs may effectively recruit spine voltage-dependent conductances[5,8,14,17,23] such as *N*-methyl-D-aspartate receptors (NMDARs) (Supplementary Fig. 1; see also Fig. 4).

We next compared the electrical properties of spines across various dendritic compartments. Owing to the inaccessibility of small-diameter oblique branches, we replaced dendritic current injection with multi-site glutamate-uncaging techniques to estimate $EPSP_{spine}$ (see Methods; Fig. 2 and Supplementary Figs 2–4, 6 and 8). We observed that the spine-to-branch AR was much lower in apical oblique dendrites than in the trunk and continued to decline significantly from originating branch points to more distal sites (Fig. 2a–e; AR: 7.8 ± 0.5, $n = 7$ spines from 7 cells for proximal sites; 3.6 ± 0.3, $n = 10$ spines from 7 cells for medial sites; and 1.7 ± 0.1, $n = 9$ spines from 6 cells for distal sites; $P < 0.0001$, one-way analysis of variance (ANOVA)). Similar ratios were found at the terminal ends of oblique dendrites (within 8 µm of the end) for EPSPs evoked with a rapid-stimulation paradigm (see Methods; Fig. 2e, red symbols; AR: 1.7 ± 0.2, $n = 12$ spines from 8 cells). Consistent with this small ratio, input onto a single spine triggered substantial Ca^{2+} signals in other nearby spines at these distal locations (Supplementary Fig. 5a–d). These data indicate that the level of passive synaptic amplification produced by R_{neck} is dependent on dendritic properties with the greatest effect at the largest compartments.

A morphologically realistic computer model was used to examine the factors involved in producing the above spatial patterns of $EPSP_{spine}$, $EPSP_{branch}$ and AR. A simple model in which the dendritic location of the input was varied while R_{neck} was held constant at 500 MΩ completely reproduced all experimental observations (Fig. 3a–c). These results indicate that the spatial profile of passive spine amplification (~30-fold decrease from trunk to branch end) reported in Fig. 2 could result solely from expected changes in local dendritic impedance[3,4,6]. When the converse simulation was implemented (that is, local dendritic impedance was held constant and R_{neck} was reduced with distance), additional implausible and experimentally unsupported manipulations were required (see Methods). This strongly suggests that R_{neck} does not systematically change across different dendritic compartments (see Supplementary Fig. 6 for intraregional variation in R_{neck}) and that the level of depolarization within the spine head is relatively independent of the local impedance profile of the dendrite (see Supplementary Equations and Supplementary Discussion). However, the size of synaptic depolarization in the parent dendrite will vary considerably (increasing ~30-fold from trunk to branch end) owing to proportional changes in the impedance of different dendritic compartments. This effect could produce the relative location independence of $EPSP_{branch}$ observed in Fig. 2f, g (ref. 24). Altogether, the presence of a large, yet modifiable, R_{neck} allows dendritic spines to function as consistent, yet adjustable, high-impedance input structures throughout the apical dendritic arborization of CA1 pyramidal neurons[14,15,25].

Of the parameters affecting dendritic impedance (axial resistance, membrane capacitance, membrane resistance) only membrane resistance is readily modulated. We therefore investigated the role of membrane resistance in spine electrical function by blocking a variety of voltage-dependent ion channels (Fig. 3d–h). Bath application of $BaCl_2$ (250–400 µM) and ZD7288 (10 µM) increased steady-state dendritic membrane resistance (measured 262 ± 33 µm from the soma) from

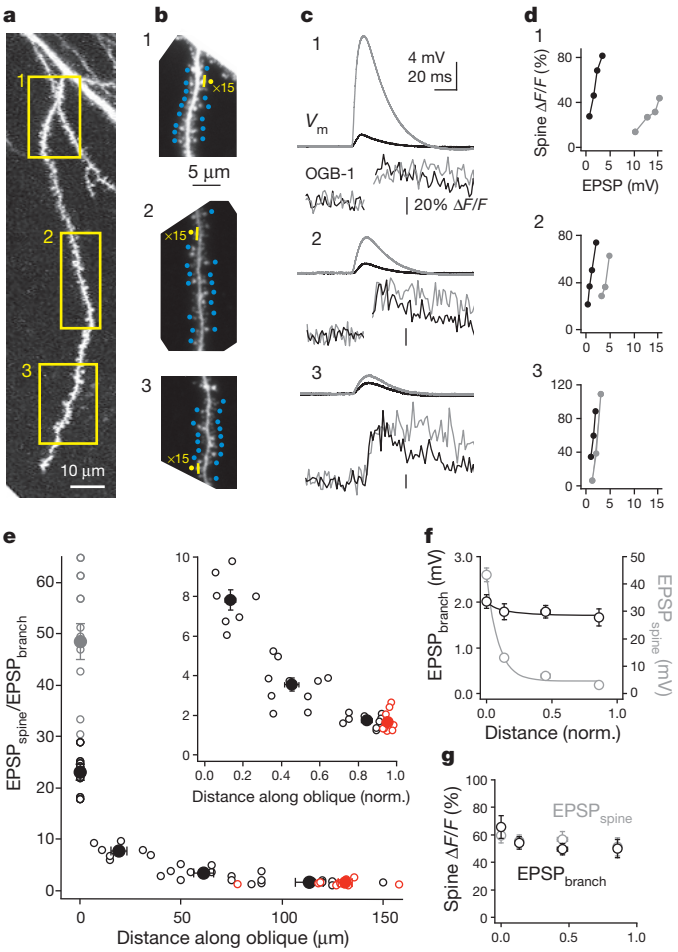

Figure 2 | Spine neck voltage amplitude ratio varies as a function of dendritic compartment. **a**, *Z*-stack image showing uncaging locations (yellow boxes) along a single apical oblique dendrite that branches from the trunk 250 µm from the soma. **b**, Increased magnification of the areas indicated in **a** showing locations for imaging (yellow line) and uncaging (yellow circles) at the spine of interest or at 15 nearby spines (blue circles). **c**, Voltage traces (recorded in the apical trunk, top) corresponding to comparable spine Ca^{2+} signals (bottom) evoked by stimulation of the spine of interest with 15 low-power uncaging pulses (black) or 15 neighbouring spines (grey) at the three input sites indicated in **a** and **b**. Note the similar EPSP kinetics for the two stimulation paradigms. **d**, Relationship between EPSP amplitude and spine head Ca^{2+} signals for single spine (black) versus neighbouring spines (grey) stimulation along the oblique branch. **e**, Spine-to-branch voltage AR as a function of dendritic compartment. Black denotes experiments conducted using uncaging at 15 neighbouring spines for $EPSP_{spine}$ (as per **a**–**d**); red indicates experiments conducted at distal tips of oblique dendrites using single stimulation of the spine of interest compared with only 1–2 neighbouring spines; and grey denotes single uncaging at trunk spines versus EPSC injection during dual dendritic recording (from Fig. 1; see Methods for discussion of different AR measurement paradigms). Inset shows AR along oblique branches as a function of normalized branch length. Open circles are data from individual spines; filled circles represent means for different compartments. **f**, Mean amplitudes of $EPSP_{branch}$ (black) and $EPSP_{spine}$ (grey) used to calculate AR as a function of normalized (norm.) distance along apical oblique dendrites for experiments conducted as described in **a**–**d**, from black data points in **e**. **g**, Corresponding mean spine head Ca^{2+} signals for $EPSP_{branch}$ (black) and $EPSP_{spine}$ (grey) from **f**. Error bars denote s.e.m.

31.6 ± 3.2 MΩ to 133.2 ± 7.7 MΩ ($P < 0.0001$, paired *t*-test, $n = 6$). As expected from theoretical considerations (see Supplementary Equations and Supplementary Discussion), this large increase in membrane resistance did not significantly alter AR (23.2 ± 1.7 versus 21.1 ± 1.5, $n = 6$ spines from 6 cells, $P = 0.097$, paired *t*-test, for trunk spines 285 ± 36 µm from soma). Additionally, manipulating resting conductance over several orders of magnitude had essentially no impact on AR

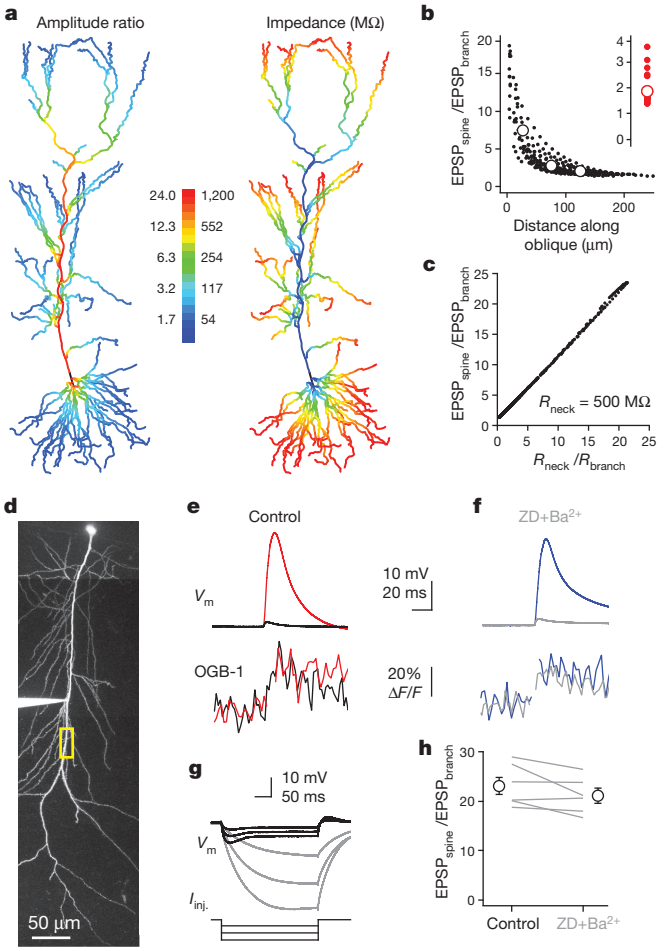

Figure 3 | Spine-to-branch voltage amplitude ratio is mediated by dendritic impedance. **a**, Left, spatial distribution of AR for spines with 500 MΩ R_{neck} in the model CA1 neuron (stimulation conducted as described for Fig. 2a–d). Right, local impedance across all compartments in the model. **b**, Modelling results for 323 spines (black dots) located on apical oblique branches that originated from the trunk 150–400 μm from the soma. Open circles represent bins of the first, second and third 50 μm along the obliques. Error bars are within the symbols. Inset shows AR for 26 model spines located within 8 μm of the tip of an oblique (as per Fig. 2e, red symbols). **c**, The degree of voltage attenuation across spine necks in the model closely matches the R_{neck}/R_{branch} ratio. **d**, Image stack of a CA1 pyramidal cell patched 215 μm from the soma. Yellow box indicates region of interest for trunk spine imaging and uncaging. **e**, Example voltage traces (top) of $EPSP_{spine}$ (red; evoked by uncaging at 30 neighbouring trunk spines) and $EPSP_{branch}$ (black; evoked by single uncaging at spine of interest) for comparable spine Ca^{2+} signals (bottom) under control conditions. **f**, Example voltage traces of $EPSP_{spine}$ (blue) and $EPSP_{branch}$ (grey) for comparable spine Ca^{2+} signals after application of 10 μM ZD7288 (ZD) and 400 μM Ba^{2+} for the same spine in **e**. **g**, Effect of ZD and Ba^{2+} on dendritic voltage responses evoked by 100–300 pA hyperpolarizing step current injections at −65 mV for the cell in **d**–**f** (control, black; ZD + Ba^{2+}, grey). **h**, Summary of the effect of ZD and Ba^{2+} on spine-to-trunk AR for six spines from six dendritic recordings. Error bars denote s.e.m.

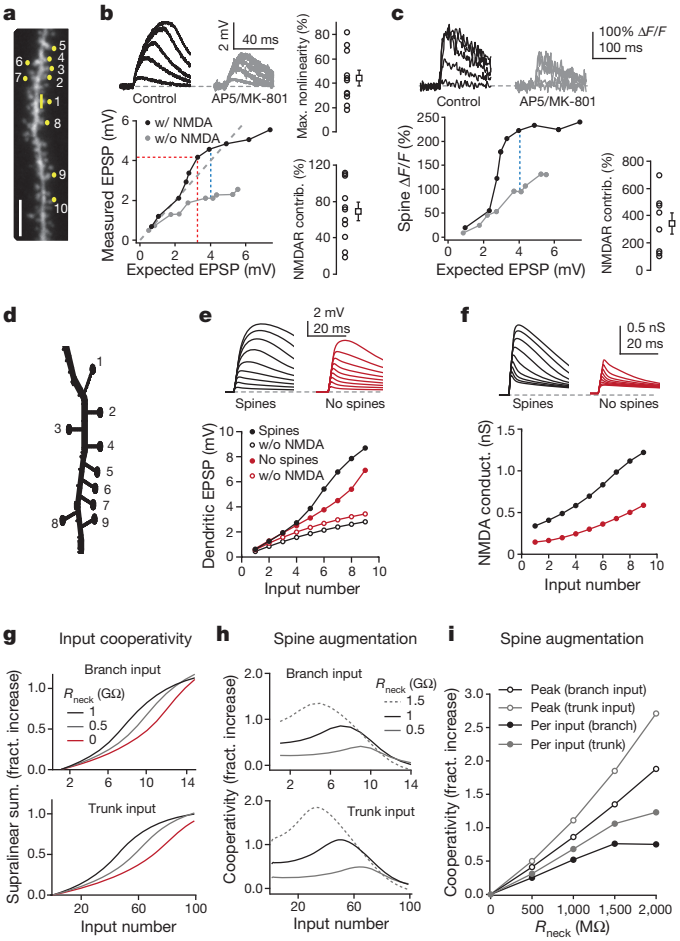

Figure 4 | Spines enhance the cooperative interaction among multiple inputs. **a**, Oblique dendrite with trunk branch point 150 μm from the soma illustrating linescan profile (yellow line) and uncaging locations (yellow dots with numbers showing sequence). Scale bar, 5 μm. **b**, Example voltage traces (top; every second trace shown) and expected versus measured EPSP plot (bottom) for uncaging at increasing numbers of spines under control conditions (black) and in the presence of NMDAR antagonists (grey), recorded at trunk. Grey dashed line indicates unity. Red dashed line indicates measurement of maximal nonlinearity (population data shown at top right, $n = 11$) and blue dashed line shows quantification of NMDAR contribution to the input–output relationship (population data shown at bottom right, $n = 11$). **c**, Example fluorescence traces (top; every second trace shown) and plot of peak $\Delta F/F$ versus expected EPSP from spine 1 during recruitment of increasing numbers of neighbouring spines under control conditions (black) and in the presence of NMDAR antagonists (grey). Blue dashed line indicates measurement of NMDAR contribution to spine head Ca^{2+} signals (population data shown at bottom right, $n = 8$). **d**, Schematic of model conditions in an oblique branch. **e**, Dendritic trunk voltage traces (top) and dendritic trunk input–output voltage relationship (bottom) with synapses onto spines (black) and onto collapsed spines (red) for the model oblique branch shown in **d**. Similar curves are shown without NMDARs present (open red and open black circles). **f**, Spine NMDAR conductance traces (top) and spine NMDAR activation versus input number (bottom) with synapses onto spines (black) and onto collapsed spines (red) for the oblique branch shown in **d**. **g**, The greater-than-linear component of input–output curves expressed as the fractional increase over linear summation for inputs ($G_{AMPAR} = 0.7$ nS; $G_{NMDAR} = 1.4$ nS) onto a terminal oblique branch or apical trunk near the branch. Input number was increased until the peak of supralinear summation was approached. **h**, Augmentation of input cooperativity by spines expressed as fractional increase in cooperativity over level achieved by no-spine input (fractional difference of $R_{neck} > 0$ and $R_{neck} = 0$ summation curves as in **g**). **i**, Spine augmentation of peak and mean input cooperativity expressed as a function of R_{neck}. Peak and mean cooperativity values are taken from plots in **h**.

in the model (see Supplementary Equations and Supplementary Discussion)[24]. These results illustrate that, in addition to R_{neck}, the most important determinants of passive spine voltage amplification are morphological factors that control the magnitude of axial current (that is, dendritic diameter as well as proximity to branch and end points). Because such factors are not easily modified, changes in R_{neck} would be the most tenable approach to altering the amplifying properties of spines[14,15].

The passive amplification capabilities of spines could potentially increase the recruitment of active voltage-dependent conductances at the site of input[5,8,14,17,23], thereby enhancing interactions among

multiple synaptic inputs. To test this idea we used multi-site uncaging and simultaneous Ca^{2+} imaging with NMDARs intact to produce voltage and single-spine Ca^{2+} input–output curves at individual apical oblique branches (Fig. 4a–c). Single inputs evoked small but detectable Ca^{2+} influx (~25% $\Delta F/F$) into activated spines and recruitment of additional inputs increased spine Ca^{2+} signals and membrane depolarization in an NMDAR-dependent nonlinear fashion (maximal EPSP nonlinearity under control: 44 ± 6%, $n = 11$ spines from 11 cells; peak difference of control versus 50–100 μM AP5 and 12.5 μM MK-801 for EPSP: 68 ± 10%, $n = 11$ spines from 11 cells; and spine head $\Delta F/F$: 344 ± 76%, $n = 8$ spines from 8 cells). These data were used to produce a multi-compartmental simulation that compared the level of cooperativity among synaptic inputs placed either onto spine compartments or directly onto dendrites (Fig. 4d–i). The simulations show that passive electrical amplification by spines promotes the recruitment of local active voltage-dependent conductances by multiple inputs, increasing the amount of above-linear summation (Fig. 4e, f). Input cooperativity, quantified as the amount of supralinear depolarization provided by additional synaptic input, increases as a function of R_{neck} (Fig. 4g and Supplementary Fig. 8). In general, this augmentation of input cooperativity by spines (expressed as the fractional increase over the no-spine condition) initially increases then declines with additional inputs (Fig. 4h). The exact relationship of spine augmentation to input number is dependent on R_{neck}, with a saturation effect beginning to occur for spines with $R_{neck} > 1.5$ GΩ (dashed line, Fig. 4h). High-impedance spines increase peak cooperativity (up to ~5×) and mean cooperativity per input (up to ~2×) as a function of R_{neck} in both large apical trunk and small terminal branch dendritic compartments (Fig. 4i; see Supplementary Fig. 7 for model parameter ranges). The presence of high-impedance spines therefore inherently augments input cooperativity by promoting electrical cross-talk between coactive synaptic inputs, providing a mechanism whereby activity-dependent changes in R_{neck} can regulate synaptic efficacy and nonlinear dendritic processing among potentiated synapses[14,15].

Our results provide insight into how the intrinsic properties of dendritic spines allow them to fundamentally shape neuronal processing and storage. Spines exhibit a high neck resistance (varying around 500 MΩ) that passively amplifies local synaptic depolarization up to 50-fold. This amplification increases the activation of voltage-dependent processes within the spine head, enhances the interaction among coactive spines, and increases nonlinear dendritic integration (Fig. 4 and Supplementary Figs 1 and 7). Furthermore, spines endow individual synapses with the ability to locally control the amount of passive (ohmic) and active (voltage-dependent conductance-based) amplification they experience through the regulation of R_{neck}[5,14,15]. The amplifying and coordinating properties of dendritic spines we have described here will have a profound effect on neuronal input processing[26], and will also influence information storage by promoting the induction of clustered forms of synaptic and dendritic plasticity among coactive spines[27–29]. Thus, spines enhance the ability of neurons to detect, uniquely respond to, and store distinct synaptic input patterns[26,30].

METHODS SUMMARY

All animal experimentation was approved by the Janelia Farm Institutional Animal Care and Use Committee and by the Animal Care and Use Committee of the Institute of Experimental Medicine, Hungarian Academy of Sciences, and was in accordance with 86/609/EEC/2 and DIRECTIVE 2010/63/EU Directives of the European Community. Full details of experimental procedures for slice preparation, patch-clamp recording, two-photon calcium imaging and uncaging, data analysis and computational modelling are provided in Methods.

Full Methods and any associated references are available in the online version of the paper.

Received 24 May; accepted 7 September 2012.
Published online 28 October 2012.

1. Ramón y Cajal, S. Estructura de los centros nerviosos de las aves. *Rev. Trim. Histol. Norm. Patol.* **1,** 1–10 (1888).
2. Bourne, J. N. & Harris, K. M. Balancing structure and function at hippocampal dendritic spines. *Annu. Rev. Neurosci.* **31,** 47–67 (2008).
3. Rall, W. Theory of physiological properties of dendrites. *Ann. NY Acad. Sci.* **96,** 1071–1092 (1962).
4. Rall, W. in *Cellular Mechanisms Subserving Changes in Neuronal Activity* (ed Woody, C. D. *et al.*) Brain Information Service Report No. 3 (Univ. of California, 1974).
5. Miller, J. P., Rall, W. & Rinzel, J. Synaptic amplification by active membrane in dendritic spines. *Brain Res.* **325,** 325–330 (1985).
6. Koch, C. & Zador, A. The function of dendritic spines: devices subserving biochemical rather than electrical compartmentalization. *J. Neurosci.* **13,** 413–422 (1993).
7. Yuste, R. Dendritic spines and distributed circuits. *Neuron* **71,** 772–781 (2011).
8. Hao, J. & Oertner, T. G. Depolarization gates spine calcium transients and spike-timing-dependent potentiation. *Curr. Opin. Neurobiol.* **22,** 509–515 (2012).
9. Guthrie, P. B., Segal, M. & Kater, S. B. Independent regulation of calcium revealed by imaging dendritic spines. *Nature* **354,** 76–80 (1991).
10. Yuste, R. & Denk, W. Dendritic spines as basic functional units of neuronal integration. *Nature* **375,** 682–684 (1995).
11. Yasuda, R. & Murakoshi, H. The mechanisms underlying the spatial spreading of signaling activity. *Curr. Opin. Neurobiol.* **21,** 313–321 (2011).
12. Chen, Y. & Sabatini, B. L. Signaling in dendritic spines and spine microdomains. *Curr. Opin. Neurobiol.* **22,** 389–396 (2012).
13. Svoboda, K., Tank, D. W. & Denk, W. Direct measurement of coupling between dendritic spines and shaft. *Science* **272,** 716–719 (1996).
14. Grunditz, A., Holbro, N., Tian, L., Zuo, Y. & Oertner, T. G. Spine neck plasticity controls postsynaptic calcium signals through electrical compartmentalization. *J. Neurosci.* **28,** 13457–13466 (2008).
15. Bloodgood, B. L. & Sabatini, B. L. Neuronal activity regulates diffusion across the neck of dendritic spines. *Science* **310,** 866–869 (2005).
16. Palmer, L. M. & Stuart, G. J. Membrane potential changes in dendritic spines during action potentials and synaptic input. *J. Neurosci.* **29,** 6897–6903 (2009).
17. Bloodgood, B. L., Giessel, A. J. & Sabatini, B. L. Biphasic synaptic Ca influx arising from compartmentalized electrical signals in dendritic spines. *PLoS Biol.* **7,** e1000190 (2009).
18. Tsay, D. & Yuste, R. On the electrical function of dendritic spines. *Trends Neurosci.* **27,** 77–83 (2004).
19. London, M. & Häusser, M. Dendritic computation. *Annu. Rev. Neurosci.* **28,** 503–532 (2005).
20. Wu, X. E. & Mel, B. W. Capacity-enhancing synaptic learning rules in a medial temporal lobe online learning model. *Neuron* **62,** 31–41 (2009).
21. Legenstein, R. & Maass, W. Branch-specific plasticity enables self-organization of nonlinear computation in single neurons. *J. Neurosci.* **31,** 10787–10802 (2011).
22. Magee, J. C. & Cook, E. P. Somatic EPSP amplitude is independent of synapse location in hippocampal pyramidal neurons. *Nature Neurosci.* **3,** 895–903 (2000).
23. Bloodgood, B. L. & Sabatini, B. L. Nonlinear regulation of unitary synaptic signals by $CaV_{2.3}$ voltage-sensitive calcium channels located in dendritic spines. *Neuron* **53,** 249–260 (2007).
24. Jaffe, D. B. & Carnevale, N. T. Passive normalization of synaptic integration influenced by dendritic architecture. *J. Neurophysiol.* **82,** 3268–3285 (1999).
25. Gulledge, A. T., Carnevale, N. T. & Stuart, G. J. Electrical advantages of dendritic spines. *PLoS ONE* **7,** e36007 (2012).
26. Branco, T., Clark, B. A. & Häusser, M. Dendritic discrimination of temporal input sequences in cortical neurons. *Science* **329,** 1671–1675 (2010).
27. Losonczy, A., Makara, J. K. & Magee, J. C. Compartmentalized dendritic plasticity and input feature storage in neurons. *Nature* **452,** 436–441 (2008).
28. Makara, J. K., Losonczy, A., Wen, Q. & Magee, J. C. Experience-dependent compartmentalized dendritic plasticity in rat hippocampal CA1 pyramidal neurons. *Nature Neurosci.* **12,** 1485–1487 (2009).
29. Harvey, C. D. & Svoboda, K. Locally dynamic synaptic learning rules in pyramidal neuron dendrites. *Nature* **450,** 1195–1200 (2007).
30. Gasparini, S. & Magee, J. C. State-dependent dendritic computation in hippocampal CA1 pyramidal neurons. *J. Neurosci.* **26,** 2088–2100 (2006).

Supplementary Information is available in the online version of the paper.

Acknowledgements We thank A. Milstein, S. Gale and R. Chitwood for help in creating analysis tools and G. Murphy, S. Williams and D. Johnston for comments on the manuscript. This work was supported by the Howard Hughes Medical Institute, the National Institutes of Health (NS-046064, NS-077601) and the Wellcome Trust (International Senior Research Fellowship to J.K.M., grant number 090915).

Author Contributions M.T.H., J.K.M. and J.C.M. conceived the project and designed the experiments. M.T.H. and J.K.M. performed all experiments and data analysis. N.S., W.L.K. and J.C.M. performed computer simulations. M.T.H., J.K.M. and J.C.M. wrote the paper with comments from all authors.

Author Information Reprints and permissions information is available at www.nature.com/reprints. The authors declare no competing financial interests. Readers are welcome to comment on the online version of the paper. Correspondence and requests for materials should be addressed to J.C.M. (mageej@janelia.hhmi.org).

METHODS

Hippocampal slice preparation. Acute, transverse hippocampal slices (400 μm) were prepared from 7–12-week-old male Sprague-Dawley and Wistar rats as described previously[27,28], according to methods approved by the Janelia Farm Institutional Animal Care and Use Committee and the Animal Care and Use Committee (ACUC) of the Institute of Experimental Medicine, Hungarian Academy of Sciences, and in accordance with 86/609/EEC/2 and DIRECTIVE 2010/63/EU Directives of the EU. In brief, animals were deeply anaesthetized with isoflurane and transcardially perfused with ice-cold cutting solution containing (in mM): sucrose 220, $NaHCO_3$ 28, KCl 2.5, NaH_2PO_4 1.25, $CaCl_2$ 0.5, $MgCl_2$ 7, glucose 7, sodium pyruvate 3, and ascorbic acid 1, saturated with 95% O_2 and 5% CO_2. The brain was quickly removed and sectioned in cutting solution with a Vibratome (Leica). Slices were incubated in a submerged holding chamber in artificial cerebrospinal fluid (ACSF) at 37 °C for 30–60 min and then stored in the same chamber at 25 °C. For recording, slices were transferred to the submerged recording chamber of the microscope where experiments were performed at 34–37 °C in ACSF containing (in mM): NaCl 125, KCl 3, $NaHCO_3$ 25, NaH_2PO_4 1.25, $CaCl_2$ 1.3, $MgCl_2$ 1, glucose 25, sodium pyruvate 3, and ascorbic acid 1, saturated with 95% O_2 and 5% CO_2. Except where described, NMDARs and voltage-gated Na^+ channels were blocked by continuous bath application of 50–100 μM AP5 (Tocris) and 0.5–1.0 μM TTX (Tocris), respectively. In some experiments, 10–15 μM MK-801 (Tocris) was also present in the ACSF; no differences were observed, so data were combined. ZD7288, nimodipine, 2-methyl-6-(phenylethynyl)-pyridine hydrochloride (MPEP), 7-(hydroxyimino)cyclopropa[b]chromen-1a-carboxylate ethyl ester (CPCCOEt), 1-naphthylacetylspermine (NASPM) (all from Tocris) and $BaCl_2$, $NiCl_2$, cyclopiazonic acid, philanthotoxin-433 (all from Sigma) were prepared as stock solutions, stored at −20 °C and diluted directly to the extracellular solution on the day of the experiment.

Patch-clamp recording. Cells were visualized using an Olympus BX-61 epifluorescent microscope equipped with infrared Dodt optics and a water-immersion lens (60×, 0.9 NA; Olympus). Current-clamp whole-cell recordings from the soma or apical dendrites of hippocampal CA1 pyramidal neurons were performed with Dagan BVC-700 amplifiers in the active 'bridge' mode, filtered at 3 kHz and digitized at 50 kHz. Patch pipettes (2–8 MΩ) were filled with a solution containing (in mM): potassium gluconate 134, KCl 6, HEPES buffer 10, NaCl 4, Mg_2ATP 4, $Tris_2GTP$ 0.3, sodium phosphocreatine 14, 0.05 Alexa 594 and 0.1 OGB-1 (Invitrogen), pH 7.25. In some experiments (Supplementary Figs 3 and 4), OGB-1 was replaced with 0.2 mM Fluo-4 or 0.2 mM Calcium Green-1 dextran conjugate (molecular mass: 70,000; both from Invitrogen). Series resistance, monitored throughout the experiment, was <30 MΩ for perisomatic recordings and ranged from 12 to 40 MΩ for dendritic recordings. All neurons had resting membrane potentials between −62 and −68 mV (dendritic recordings) or −56 and −65 mV (somatic recordings) and were confirmed to have intact somas and tufts. For simulated EPSC injection during dual dendritic trunk recording (Fig. 1) we used a simple compartment model of a spine, spine neck and parent branch implemented in the neuron modelling environment to determine the appropriate kinetics for current injection into the dendrite to mimic synaptic depolarization in the spine head. The resulting waveform is shown in Fig. 1c.

Two-photon imaging and uncaging. A dual galvanometer-based two-photon laser scanning system (Prairie Technologies) was used to image neurons and to focally uncage glutamate at individual dendritic spines[27,28]. Two ultrafast pulsed laser beams (Chameleon Ultra II; Coherent) were used: one at 880 and 920 nm for imaging Alexa 594 and OGB-1 (Molecular Probes), respectively, and one at 720 nm to photolyse 4-methoxy-7-nitroindolinyl-caged-L-glutamate (MNI-glutamate) (Tocris Cookson; 10 mM, dissolved in freshly carbogenated ACSF containing 50–100 μM AP5 and 0.5–1.0 μM TTX unless otherwise noted and applied via pressure ejection through a pipette above the slice). Laser beam intensity was independently controlled with electro-optical modulators (model 350-50; Conoptics). Uncaging dwell time was 0.2 ms; galvo move time intervals varied depending on the experiment (see below). Linescan imaging through spines was performed at 150–500 Hz with dwell times of 8–12 μs for <400 ms.

Particular care was taken to limit photodamage during imaging and uncaging. This included the use of a passive 8× pulse splitter in the uncaging path in most experiments to reduce photodamage drastically[31]. Basal fluorescence of both channels was continuously monitored as an immediate indicator of damage to cellular structures. Subtle signs of damage included decreases in or loss of phasic Ca^{2+} signals in spine heads in response to either uncaging or current injection, small but persistent depolarization following uncaging, and changes in the kinetics of voltage responses to uncaging or current injection. Experiments were terminated if neurons exhibited any of these phenomena.

Determination of AR and R_{neck}. Our experimental strategy was based on the biophysical property of asymmetric voltage attenuation across the spine neck due to the high impedance of the spine head relative to the low dendritic branch input impedance[4,6,32]. Thus, EPSP-shaped voltage transients substantially attenuate only as they propagate out of the spine and into the dendrite. We exploited this feature to compute an AR for EPSPs initiated in the spine and measured in the dendrite ($EPSP_{branch}$; so called because the measured EPSP amplitude reflects the spine potential after it has propagated across the spine neck into the branch) compared to those producing the same level of spine depolarization when initiated and measured in the dendrite ($EPSP_{spine}$; representing the EPSP amplitude in the spine head). Our computer model confirmed that AR magnitude is independent of the electrical recording site and that this method is sufficiently accurate to measure spine voltage AR throughout the CA1 dendritic arborization within the stratum radiatum (Supplementary Fig. 8).

For the dual dendritic patch experiments shown in Fig. 1, the EPSPs evoked by uncaging at single spines exhibited an almost identical amplitude at both pipettes (1.41 ± 0.16 versus 1.44 ± 0.15 mV, $n = 9$, $P = 0.3032$, paired t-test), demonstrating that the base of the dendrite at nearby spines is isopotential with the recording electrode. In addition, our morphologically realistic multi-compartmental model suggests that the trunk should be relatively isopotential to ~30 μm proximal (towards the soma) and ~50 μm distal from the electrode.

Calculation of R_{neck} is based on the voltage divider equation[4,32] (see Fig. 1h). EPSP amplitude at the spine head for a synapse on the spine is given by:

$$V_{head} = E_{syn.} \frac{R_{neck} + R_{dend.}}{1/G_{syn.} + R_{neck} + R_{dend.}} \quad (1)$$

in which V_{head} is the EPSP amplitude in the spine head and $R_{dend.}$ is local dendritic input resistance.

EPSP amplitude at the dendrite for a synapse on the spine is given by:

$$V_{dend.} = E_{syn.} \frac{R_{dend.}}{1/G_{syn.} + R_{neck} + R_{dend.}} \quad (2)$$

in which $V_{dend.}$ is the EPSP amplitude in the dendrite.

The ratio of the amplitudes (AR) is given by:

$$AR = \frac{R_{neck} + R_{dend.}}{R_{dend.}} = 1 + \frac{R_{neck}}{R_{dend.}} \quad (3)$$

The resistance of the spine neck (R_{neck}) can be calculated from:

$$R_{neck} = (AR - 1) \times R_{dend.} \quad (4)$$

Uncaging input paradigms. Because we cannot patch small diameter terminal branches, in order to measure AR in these compartments, local dendritic current injection (as used in Fig. 1) was replaced with rapid multi-site glutamate uncaging onto neighbouring spines near the spine of interest while recording the resultant EPSPs at the apical trunk (Figs 2 and 3e and Supplementary Figs 3, 4 and 6c–f) or soma (Supplementary Figs 2a–c and 6a, b). The speed at which each spine on a dendrite can be stimulated is limited by the uncaging galvanometers (in practice this is 0.3 ms per spine: 0.2 ms dwell time + 0.1 ms move time). Thus, to control for possible confounds in differential dendritic filtering along oblique branches, we matched the shape of depolarizations for $EPSP_{branch}$ and $EPSP_{spine}$ measured at the voltage-recording electrode by using 15 (low-power) uncaging events at the single spine of interest versus 15 (higher power) uncaging events distributed at 15 neighbouring spines on the same branch (Fig. 2 and Supplementary Figs 3 and 4). The branch uncaging input was performed at the galvanometer speed limit while the galvanometer move time was occasionally increased (up to 0.3 ms) for the 15 uncaging events at the single spine in order to match the kinetics of the two EPSPs. The computer model indicates that the kinetic slowing associated with this method decreased observed AR ~50% at dendritic trunk regions (Supplementary Fig. 8a; thus the AR values of ~22 for the trunk experiments conducted in this manner in Fig. 2e compared to the AR of ~45 measured by comparing a single uncaging event with fast current injection in Fig. 1) and ~15% at terminal branch locations (Supplementary Fig. 8b). However, at the distal tip of oblique branches, where the dendritic impedance is high owing to the sealed end, we were able to conduct experiments comparing a single uncaging event at the spine of interest to uncaging at only 1–2 nearby neighbours (see Supplementary Fig. 5a–d) for the calculation of AR in this compartment (Fig. 2e, red symbols). Thus, we have accurate fast kinetic boundary conditions for AR at the trunk (using current injection, Fig. 1) and the distal dendritic tip (using 1–2 neighbouring spines; Fig. 2e, red symbols) while the exact shape of the distribution of AR along the branch will vary slightly depending on the frequency of the stimulation protocol. For some experiments measuring the relative effects of pharmacology on AR, we compared a single uncaging event at the spine of interest with uncaging at a number of neighbouring spines (Fig. 3e and Supplementary Fig. 2b).

Data analysis. Analysis was performed using custom-written macros in IgorPro and MATLAB. Ca^{2+} and voltage signals were analysed offline using averaged traces of 3–10 trials with no smoothing or background subtraction. Some imaging trials exhibited a light artefact from the uncaging laser, which was excised. Ca^{2+} signal amplitude was measured as the maximum average of three consecutive points within 50 ms after uncaging. For calculation of AR, spine Ca^{2+} signals greater than 25% and less than 125% $\Delta F/F$ (the linear range of OGB-1; Invitrogen) were compared between stimulation paradigms at a range of different intensities. For branch versus spine Ca^{2+} signals exhibiting less than 25% difference (average difference of 3.1 ± 1.5%, $n = 109$ spines from 71 neurons; see also Supplementary Fig. 9) their respective EPSPs (larger than 1 mV for trunk spines recorded at the trunk <50 μm away, or larger than 0.5 mV for oblique spines recorded at the trunk or soma) were compared. All comparisons that fit these criteria for a given spine were averaged to compute the AR for that paradigm at that spine.

Morphological and distance measurements were performed using ImageJ/FIJI (National Institutes of Health) on two-dimensional maximal intensity projections of 1–2 μm *Z*-series collected at the end of the experiment. Spines on apical oblique branches were categorized as proximal, middle or distal by division of the overall branch length into thirds.

Owing to the necessity of clearly isolating a single spine for uncaging in order to accurately calculate AR (if multiple spines are activated by a single uncaging event, $EPSP_{branch}$ becomes artifactually large compared to the observed spine head Ca^{2+} signal and distorts the AR), spines chosen for imaging were clearly separated from their parent dendrite (and nearby neighbours). Individual spines were selected to reflect the average phenotype of their neighbours along a branch, and did not exhibit overly large heads or long necks, presumably falling into an intermediate category between or spanning the previously described 'stubby' and 'mushroom' types. At the beginning of an experiment, Ca^{2+} signals in response to single-spine uncaging at various laser powers were first measured and only those spines in which the Ca^{2+} signal and EPSP amplitude increased incrementally as a function of power were further studied. This criterion was met in most spines of the apical trunk and oblique dendrites. However in a subgroup of spines, primarily on oblique branches, Ca^{2+} signals were either small and unreliable or did not increase proportional to increasing stimulation. These recordings were not included in this study. For the long spine neck experiments in Supplementary Fig. 6a, b, we searched the dendritic arborization for the longest-necked spines we could find (which appeared to constitute <1% of the overall spine population).

Computational methods. All simulations were performed using the NEURON simulation environment[33] with the variable time step (CVODE) method. The CA1 pyramidal neuron morphology used in the simulations was reconstructed from a rat hippocampal pyramidal neuron described previously[34,35]. The model included a membrane capacitance of 1 μF cm^{-2} and an axial resistivity of 150 Ω cm. The membrane resistivity was taken to be 20,000 Ω cm^2 at the soma and to drop linearly as a function of distance to 2,500 Ω cm^2 at a distance of 100 μm and beyond to reflect, in a simple way, the observed greater density of voltage-gated channels observed experimentally in these cells[36,37]. As a result, the somatic input resistance was observed to be 27 MΩ, and the input resistance 200 μm from the soma along the main apical dendrite was 23 MΩ.

A second model (uniform $R_{dend.}$ model) was constructed to produce a relatively constant local dendritic input impedance along apical oblique branches while maintaining the measured amount of amplitude filtering down the branches. This required reductions in both axial and membrane resistivity coordinated with dendritic diameter, implemented through gradients of axial (from 28 to 150 Ω cm; branch tip to trunk) and membrane resistivities (from 28 to 2,500 Ω cm^2; branch tip to trunk) in a specific oblique dendrite (branching from the main apical dendrite approximately 300 μm from the soma) according to the following formulae:

$$r_L(x) = r_L(0)[a(x)/a(0)]^{\alpha}$$

and

$$r_m(x) = r_m(0)[a(x)/a(0)]^{\beta}$$

in which x is the distance along the oblique branch measured from the main apical dendrite, r_L is axial resistivity, r_m is membrane resistivity, a is dendrite diameter, and $\alpha = 1.5$, $\beta = 4$. The selected branch had an approximately constant input impedance over most of its length (~50–60 MΩ over ~200 μm). This model could reproduce the observed dependence of AR upon distance along the oblique dendrite if R_{neck} was also dependent upon distance. A prediction for the required R_{neck} can be computed from

$$R_{neck} = (AR - 1)R_{dend.}$$

in which AR is the desired target amplitude ratio and $R_{dend.}$ is the dendritic input impedance. R_{neck} for this condition ranged from 39.7 to 465.1 MΩ from tip to trunk. A variable increase in synaptic conductance approaching tenfold (20 to 2.0 nS from tip to trunk) was also required to match data shown in Fig. 2d. However, in the uniform R_D model several key fundamental electrophysiological properties move far out of reported experimental ranges. First, the membrane time constant becomes very small (<100 μs) because of the large leak conductance. Reported experimental measures are two orders of magnitude larger[36]. Second, the impedance load of each dendrite branch increases considerably causing enhanced attenuation of signals propagating from dendrite to soma. In the standard model the maximum amount of attenuation from the distal apical trunk to the soma was 6.4, whereas in the uniform $R_{dend.}$ model the level of attenuation was 46.9. Finally, the manipulations caused the input resistance at the soma to drop to 6 MΩ. These values are both approximately an order of magnitude out of the range of what has been observed experimentally[36]. Altogether, the need for coordinated 5–10× manipulations of axial resistivity, membrane resistivity, R_{neck} and synaptic conductance contradicts experimental evidence[38] and is extremely implausible.

In both models, spines were modelled as a cylindrical compartment representing the spine neck with length 1.58 μm and diameter 0.077 μm and a spherical head with diameter 0.5 μm; with an axial resistivity of 150 Ω cm, this produced a R_{neck} of 500 MΩ. Simulations of spines placed directly on the dendrite were modelled by reducing the neck length to 0.01 μm and increasing the diameter to 0.5 μm (to match the spine head diameter). AMPA synapses were modelled as a double-exponential conductance function with rise time 0.1 ms, decay time 1 ms and reversal potential 0 mV. For simulations involving only AMPA synapses, the peak conductance was adjusted dynamically at each location in the dendritic tree using a root-finding algorithm[39] to reach a target depolarization in the spine head of 35 mV; results were not strongly dependent upon the specific target voltage used. Modelling of low-power multi-event or rapid multi-site glutamate uncaging was performed computationally by activating a series of synapses with a 0.3-ms delay between events. To speed up simulations of single-site multiple events, the series of double-exponential AMPA conductances was replaced with a single, averaged conductance. To do the averaging, one starts with a double-exponential synapse that turns on at the source time s,

$$g = g_{max.} C(e^{-(t-s)/\tau_2} - e^{-(t-s)/\tau_1}) \text{ for } t > s$$

The constant C is chosen so that the maximum of the right-hand side is g_{max}. Note that here we are assuming that $\tau_1 < \tau_2$. τ_1 is the rise time and τ_2 is the decay time. If we now suppose that synapses are distributed over the time interval $0 < s < T$ with conductance $g_{max} = g(s)ds$, and we add up these individual contributions,

$$g = \int_0^{\min(t,T)} g(s)C\left(e^{-(t-s)/\tau_2} - e^{-(t-s)/\tau_1}\right)ds$$

Note the upper limit $\min(t,T)$ is due to causality; for $t < T$ one only has contributions for $0 < s < t$; when $t > T$; however, one gets contributions for the whole range, $0 < s < T$. If one assumes a uniform distribution of synaptic strength over time (that is, each successive uncaging event elicits exactly the same amount of synaptic response), one can take $g(s) = 1$ and evaluate the integral. The result is

$$g/C = \tau_2(1 - e^{-t/\tau_2}) - \tau_1(1 - e^{-t/\tau_1}) \text{ for } t < T,$$

$$g/C = \tau_2(1 - e^{-T/\tau_2})e^{-(t-T)/\tau_2} - \tau_1(1 - e^{-T/\tau_1})e^{-(t-T)/\tau_1} \text{ for } t > T$$

The maximum of this function can be determined and C chosen to normalize the conductance. Because it was found that computational models of rapid multi-site glutamate uncaging depended very weakly upon spine location, as long as spines were within a spatial range of a few tens of μm of one another, the above averaged conductance was also used to simulate multi-site glutamate uncaging. AR can depend strongly on the additional time interval over which synaptic current is distributed. Supplementary Fig. 8 shows the result of simulations for a synapse on a spine located either on the main apical trunk approximately 200 μm from the soma, or on an apical oblique dendrite roughly 80% of the distance along the oblique from the trunk to the tip of the oblique. For the case of the spine on the apical trunk, as the time interval T increases from 0 to 6 ms, the AR decreases from more than 40 to approximately 20. Further increases in the time interval cause relatively small further decreases in the AR, as the value asymptotes to the AR for steady-state currents. For the case of the spine on the oblique, the AR is largely independent of the spread time of the synaptic current. In simulations including NMDAR synapses, the AMPA conductance was set at 0.7–1 nS. NMDAR synapses were modelled as a double-exponential conductance function with rise time 1 ms, decay time 75 ms, peak 1.4–3.0 nS and reversal potential 0 mV. In addition, for NMDAR synapses a voltage-dependent factor

$$g(V) = \frac{1}{1 + \exp.(-0.062V[\mathrm{Mg}]/3.57)}$$

multiplied the total conductance, in which V is the membrane potential in mV, and [Mg] is the extracellular magnesium concentration in mM, to model the relief of the voltage-dependent magnesium block of NMDA channels. A magnesium concentration of 1 mM was used in all simulations.

31. Ji, N., Magee, J. C. & Betzig, E. High-speed, low-photodamage nonlinear imaging using passive pulse splitters. *Nature Methods* **5,** 197–202 (2008).
32. Johnston, D. & Wu, S. *Foundations of Cellular Neurophysiology* Ch. 13, 400–411 (MIT Press, 1995).
33. Hines, M. L. & Carnevale, N. T. The neuron simulation environment. *Neural Comput.* **9,** 1179–1209 (1997).
34. Golding, N. L., Kath, W. L. & Spruston, N. Dichotomy of action-potential backpropagation in CA1 pyramidal neuron dendrites. *J. Neurophysiol.* **86,** 2998–3010 (2001).
35. Golding, N. L., Mickus, T. J., Katz, Y., Kath, W. L. & Spruston, N. Factors mediating powerful voltage attenuation along CA1 pyramidal neuron dendrites. *J. Physiol. (Lond.)* **568,** 69–82 (2005).
36. Magee, J. C. Dendritic Ih normalizes temporal summation in hippocampal CA1 neurons. *Nature Neurosci.* **2,** 508–514 (1999).
37. Hoffman, D. A., Magee, J. C., Colbert, C. M. & Johnston, D. K. K^+ channel regulation of signal propagation in dendrites of hippocampal pyramidal neurons. *Nature* **387,** 869–875 (1997).
38. Katz, Y. *et al.* Synapse distribution suggests a two-stage model of dendritic integration in CA1 pyramidal neurons. *Neuron* **63,** 171–177 (2009).
39. Dowell, M. & Jarratt, P. A modified regula falsi method for computing the root of an equation. *Bit Numerical Mathematics* **11,** 168–174 (1971).